

On-chip transporting arresting and characterizing individual nano-objects in biological ionic liquids

Journal Article**Author(s):**

Höller, Christian; [Schnoering, Gabriel](#) ; Eghlidi, Hadi; Suomalainen, Maarit; Greber, Urs F.; Poulidakos, Dimos

Publication date:

2021-06-30

Permanent link:

<https://doi.org/10.3929/ethz-b-000493443>

Rights / license:

[Creative Commons Attribution-NonCommercial 4.0 International](#)

Originally published in:

Science Advances 7(27), <https://doi.org/10.1126/sciadv.abd8758>

APPLIED SCIENCES AND ENGINEERING

On-chip transporting arresting and characterizing individual nano-objects in biological ionic liquids

Christian Höller^{1†}, Gabriel Schnoering^{1†}, Hadi Eghlidi¹, Maarit Suomalainen², Urs F. Greber², Dimos Poulikakos^{1*}

Understanding and controlling the individual behavior of nanoscopic matter in liquids, the environment in which many such entities are functioning, is both inherently challenging and important to many natural and man-made applications. Here, we transport individual nano-objects, from an assembly in a biological ionic solution, through a nanochannel network and confine them in electrokinetic nanovalves, created by the collaborative effect of an applied ac electric field and a rationally engineered nanotopography, locally amplifying this field. The motion of so-confined fluorescent nano-objects is tracked, and its kinetics provides important information, enabling the determination of their particle diffusion coefficient, hydrodynamic radius, and electrical conductivity, which are elucidated for artificial polystyrene nanospheres and subsequently for sub-100-nm conjugated polymer nanoparticles and adenoviruses. The on-chip, individual nano-object resolution method presented here is a powerful approach to aid research and development in broad application areas such as medicine, chemistry, and biology.

INTRODUCTION

Controlling the motion and determining the properties of nanoscopic objects in liquids, from synthetic to biological, is of great scientific and also practical interest in diverse fields such as biology and medicine (1–6), nanorobotics (7, 8), and chemistry (9). As a result, a host of approaches are being developed, targeting the elusive manipulation and characterization of single nanoscale objects. These approaches often rely on the designed interaction of particles with an external force field, being fluidic (10), optical (11–13), or electrical (14), to overcome the predominant inherent thermal fluctuations. For example, optical near fields can confine bioparticles of just a few nanometers either in the middle of a nano-aperture (15) or, combined with fluidic effects, on the edge of a plasmonic array (16).

For particles diffusing in micro- and nanochannels, electrostatic and electrokinetic approaches have been successfully implemented with charged nanoparticles in liquids at nonbiological, low ionic strengths. They were used to trap, valve, or sort nano-objects of different sizes (17–21). In contrast, the present work, in addition to trapping and manipulation, focuses on size and property measurements at high, biological level, ionic concentrations, which would be outside the realm of reliable trapping capabilities of reported static, electric double layer–based trapping approaches at these sizes (17). Working with biological particles in their natural environment, on the other hand, requires highly ionic media (22) in which electrostatic wall forces are practically shielded by the electrical double layer and restricted to short distances of just a few nanometers away from the walls (14). In such media, the diffusion of particles in nanopores allows their counting and size determination with applied currents in the fluid (23, 24). Yet, control and knowledge of their motion greatly improves with imposed electrokinetic forces on a nano-object to enable their manipulation (18, 25–27). This allows the trapping and manipulation of nanoparticles as small as a few nanometers. In

terms of measuring properties and following their kinetic behavior, as done in this work, there are additional limitations on visibility (sufficient fluorescence signal) and the long-term mechanical stability of the experiment with an on-chip system upscalable as presented here. To this end, the lower limit in terms of measuring properties reliably would be one order of magnitude larger, hence, of the order of a few tens of nanometers.

In this work, we go well beyond kinetic control of single nano-objects in highly ionic environments and are able to realize directly and non-intrusively their characterization, by means of determining their important fundamental properties. We use a pair of ac electrokinetic nanovalves in a nanochannel that are amplified by a specifically designed and fabricated channel restriction nanotopography to arrest nano-objects. The nanotopography can generate a dielectrophoretic linear restoring force on the trapped particle whose motion is then well described by a harmonic potential. The confined kinetics of the nano-object is measured at speeds much faster than the characteristic time scale of diffusion, and in combination with theoretical analysis, the particle diffusion coefficient, hydrodynamic radius, and electrical conductivity are determined. In addition to known size polystyrene (PS) beads, we investigate two types of nano-objects in their native (high ionic strength) environment: adenoviruses and conjugated polymer nanoparticles (CPNs), crucial for biomedical and virology applications.

RESULTS

Stable confinement in-between ac electrokinetic nanovalves along the channel

Individual nanoparticles moving in biologically relevant solutions are transported and manipulated to assess their key properties. To do this, we use a nanofluidic channel supplemented with insulated nanoelectrodes on either side of nanofabricated steps as illustrated on Fig. 1A. This combination generates a strong, controllable, electrokinetic force, when applying an ac voltage V , typically 2 V at 10 MHz. Experiments are performed in high ionic strength solutions where a dielectric particle in an ac electric field gradient is repelled from the denser region of the field. Consequently, the downstream

Copyright © 2021
The Authors, some
rights reserved;
exclusive licensee
American Association
for the Advancement
of Science. No claim to
original U.S. Government
Works. Distributed
under a Creative
Commons Attribution
NonCommercial
License 4.0 (CC BY-NC).

¹Laboratory of Thermodynamics in Emerging Technologies, ETH Zurich, Sonneggstrasse 3, Zurich, Switzerland. ²Institute of Molecular Life Sciences, University of Zurich, Zurich, Switzerland.

*Corresponding author. Email: dpoulikakos@ethz.ch

†These authors contributed equally to this work.

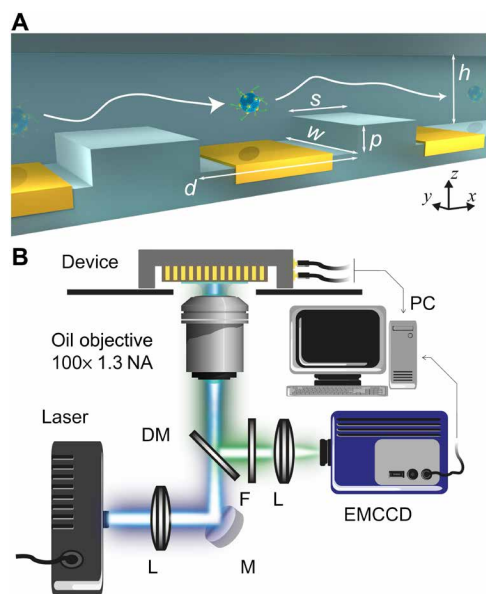


Fig. 1. Electrokinetic valves experimental setup. (A) Schematic of the electrokinetic nanovalve system that enables the confinement and measurement of single nano-objects. The 300-nm-high and 500-nm-wide nanochannel allows the generation of a dielectrophoretic force between the electrodes when driven by an ac voltage. A 100-nm-high dielectric step between the electrodes increases the electric field locally and amplifies the force exerted on a particle in the nanochannel. This creates an impenetrable barrier for the particle. Placing two such valves close to each other creates a confinement zone on top of the electrode shared by both valves. The controlled confinement and release of particles, here illustrated by a virus drawing, is performed by opening and closing the valves. (B) The motion of the particle is recorded by a fast and sensitive camera (Andor iXon Ultra 888). The camera records the fluorescence emitted by the particle, which is excited by a blue laser (460 nm). The blue light is focused with a lens (L) at the back-focal plane of an oil immersion objective [Olympus 100x, 1.3 numerical aperture (NA)] illuminating homogeneously the confinement volume. Light emitted by the particle is collected by the objective, separated from illumination by a dichroic mirror (DM) and a band-pass filter (F), and then sent to the camera. Acquisition of the video and operation of the valves are synchronously controlled by a computer.

motion of a particle is stopped by an ac electrokinetic barrier, manifesting itself through the corresponding dielectrophoretic force, which is applied at will, functioning as a switchable nanovalve (18). Two such valves are placed close together in series within the channel frame, an active confinement region in between (Fig. 1A). At the starting point of an experiment, one (upstream) confining valve is open, while the second (downstream) is closed. A single particle moves through the open valve and enters the confinement region (i). Next, the open valve is closed, and the particle is effectively trapped between the valves (ii). The confined dynamics of the nano-object in this location is then recorded and analyzed, which eventually enables the determination of important nano-object properties related to its motion. Last, after characterization of the particle, the downstream valve is opened, and the particle moves out of the confinement region (iii), freeing the system for the next particle.

The nanofluidic channel is carved in a silicon oxide layer at the surface of a silicon wafer. Fabrication of the system requires a number of lithography steps, which are needed to create the desired nanotopographic features and the insulated gold electrodes placed in the nanochannels. Details of the general fabrication protocol can be

found in (18). The nanochannels and the supporting integrated circuit stand upside down on a motorized stage on top of an inverted microscope as depicted in Fig. 1B. The channel is aligned such that the volume between two valves, where particles are confined, is clearly imaged. Nano-objects studied in this work are fluorescent and excited using a blue laser diode (460 nm) focused at the back-focal plane of a high-magnification oil immersion objective (100x, 1.3 numerical aperture) to provide a homogeneous illumination over the confinement area. The exciting blue light is attenuated to provide a faint intensity of only 85 μ W at the entrance of the objective to avoid light-induced heating. The fluorescent light emitted by the particle is recaptured by the objective, separated from the illumination by a dichroic mirror (cutoff at 490 nm) and a band-pass filter (500 to 600 nm), and then sent to a camera. A fast and sensitive camera [Electron multiplying charge coupled device (EMCCD)] records the fluorescence signal at speeds up to 1000 Hz. Acquisition of the video and operation of the valves are synchronously controlled by a computer.

The dynamics of a particle in the electrokinetic valve is first illustrated by confining and recording the motion of a single fluorescent PS nanosphere, with a 50-nm radius, initially in a mixture of identical beads, and suspended in 0.1x phosphate-buffered saline (PBS) at room temperature $T = 294$ K, taking advantage of the sensitivity of the particle conductivity to radio frequencies (10 MHz). We also note that Joule heating is negligible during system operation (18) as well as photothermal effects induced by the fluorescent particle (note S6) (28, 29). The instantaneous position projected on the xy plane is extracted from the recorded videos by motion tracking of the point spread function using a Gaussian filter, offering subpixel resolution (30). The typical position evolution (over 10 s) of a confined particle between the valves is illustrated in Fig. 2A as a sequence of positions, each separated by 1 ms in time. The nanochannel has a width $w = 500$ nm and a height $h = 300$ nm. Above the fabricated topographic steps ($p = 100$ nm), the channel height is reduced to 200 nm, while the width remains the same (Fig. 2A). The space between two consecutive steps containing an electrode is $d = 600$ nm. The particle motion dynamics within the confinement volume for three different voltages V is presented in Fig. 2 (B and C), as position density histograms for displacements in the x and y directions, respectively. A clear dependence in the applied voltage is apparent for the x motion along the channel, while the perpendicular y motion is independent of the field strength. The position probability density in the direction of the channel axis has a Gaussian shape, which narrows significantly in going from 1.4 to 2.2 V in applied voltage V , sharpening accordingly the imparted confinement. At 2.2 V, the deviation of the Gaussian is as small as 42 nm. The motion of the particle in the transverse y direction experiences only the confinement exerted by the walls, and the particle explores the space in this direction practically uniformly. This exploration includes direct interaction with walls characterized predominantly by short-distance electrostatic forces and becomes negligible approximately 15 nm away from surfaces (14). The position probability density uniformity is in the range of ± 200 nm.

Dielectrophoretic force under ac frequency

In the following, the voltage-dependent motion along the main particle propagation x is studied, where the electric potential V imposes a direct and tunable control over the confinement of the particle as shown in Fig. 2 (B and C) and where the aim is to regulate the particle transport. The 10-MHz ac electric potential applied to the electrodes

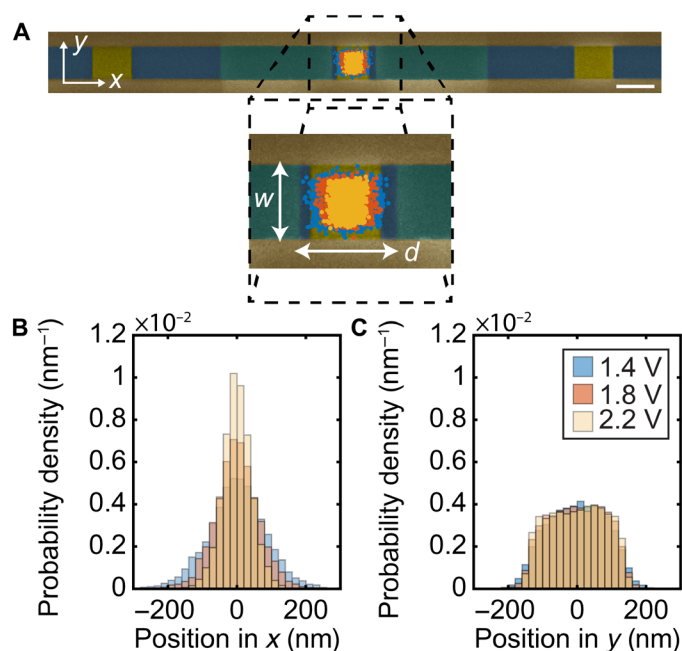


Fig. 2. Recorded positions and statistics of a confined 100-nm polystyrene sphere in the nanochannel. (A) False-colored scanning electron microscopy image of the nanochannel with the recorded measured positions of a 100-nm PS bead superimposed. The bottom of the channel is depicted in dark blue and the side walls, at a distance of $w = 500$ nm, in brown. Three electrodes, forming two valves, are shown in gold color and the two fabricated steps, separated by $d = 600$ nm, on each side of the central electrode in green. Successive positions (recorded for 10 s at 1000 Hz) of a confined PS sphere are overlaid, for ac potentials of 2.2 (yellow), 1.8 (red), and 1.4 V (blue), respectively. The white scale bar is 500 nm. (B and C) The position probability density in the axial (x axis) and transverse (y axis) channel directions. The position probability density in the axial direction of the channel has a Gaussian shape and becomes narrower with increasing ac potentials. In the transverse direction, the particle only experiences the confinement of the walls and explores uniformly the space.

generates a time-averaged field intensity $|E(x)|^2$ that acts on the confined particle. Because we are working with a high ionic strength fluid, electrostatic contributions from the channel walls are screened and have a negligible effect on the particle motion in the axial x direction of the channel. The dominant electrokinetic force is the time-averaged ac dielectrophoretic force, which, for a spherical equivalent of a particle, is given by (14)

$$F_{\text{DEP}}(x) = 2\pi\epsilon_m r^3 \text{Re}[\text{CM}] \nabla |E(x)|^2 \quad (1)$$

where ϵ_m is the electrical permittivity of the medium, r is the particle hydrodynamic radius, and $\text{Re}[\text{CM}]$ is the real part of their Clausius-Mossotti (CM) factor. At our operating conditions, in high ionic solutions with an electric field alternating at 10 MHz, the real part of the CM factor reads (note S1)

$$\text{Re}[\text{CM}] \approx \frac{\sigma_p - \sigma_m}{\sigma_p + 2\sigma_m} \quad (2)$$

depending only on the known medium electrical conductivity σ_m and the unknown nano-object electrical conductivity σ_p , which is

hence determined if $\text{Re}[\text{CM}]$ is obtained from the gathered kinetics data. At the frequency of 10 MHz, despite its seemingly high value, $\text{Re}[\text{CM}]$ is still dominated by the particle and medium conductivities while simultaneously suppressing ac electro-osmosis (note S1) (14, 18). Our working frequency, combined with the thin double layer due to the high ionic concentration, ensures that the polarizability of the particles originates from the external field only without flow-induced contributions (31, 32). This is achieved by designing the time-averaged ac dielectrophoretic force, $F_{\text{DEP}}(x)$, to be a linear restoring force with respect to x , as will be discussed later.

Langevin equation of motion and linearization of ac dielectrophoretic force

The motion of the particle in the confinement space is subject to three forces and is well described by the overdamped Langevin equation. Specifically, these forces are the inherent time-dependent thermal force $F_{\text{th}}(t)$ driving the Brownian motion; the frictional fluidic drag force $F_{\text{drag}} = -\gamma\dot{x}$, resisting motion, where γ is the time-averaged drag coefficient; and the confining dielectrophoretic force in $F_{\text{DEP}}(x)$ (Eq. 2), which yields

$$\gamma\dot{x} = F_{\text{DEP}}(x) + F_{\text{th}}(t) \quad (3)$$

In the uncorrelated stochastic thermal force $F_{\text{th}}(t) = \sqrt{2\gamma k_B T} \Gamma(t)$, $\Gamma(t)$ is a random Gaussian process such that $\langle \Gamma(t) \rangle = 0$ and $\langle \Gamma(t) \Gamma(t') \rangle = \delta(t - t')$. All three studied types of particles have shapes closely approximated by a sphere. We assume all studied nano-objects as spherical and of constant size over the course of the experiment. The measured drag coefficient γ is related to the Stokes law by $\gamma_S = \Phi\gamma$, where $\gamma_S = 6\pi\eta r$ is the Stokes drag coefficient for a freely diffusing sphere of hydrodynamic radius r in bulk water of known viscosity η and Φ is an averaged scaling coefficient to the confined diffusion in the nanochannel and is discussed in detail in note S2.

It is apparent from (Eqs. 1 and 3) that the overall dynamics of a nano-object subjected to the ac dielectrophoretic force $F_{\text{DEP}}(x)$ is strongly affected by the gradient of the electric field intensity $\nabla |E(x)|^2$, to which this force is proportional. On the basis of this, the nanochannel topography is designed and fabricated such that, while it is geometrically simple, (i) it significantly increases the gradient $\nabla |E(x)|^2$ and (ii) it renders this gradient to be linear with respect to the displacement x in the confinement region. As shown below, the resulting linearity of the restoring force F_{DEP} provides an expression for the motion of the confined nano-object and a direct measurement of the confinement strength, the trap stiffness.

As detailed in note S1, the relative position and sizing of the topographic steps and electrodes are designed with the help of numerical simulations to yield a parabolic electric field intensity in the nano-object confinement region, such that $|E(x, V)|^2 = \alpha(V)^2 x^2$, with $\alpha(V)$ as a proportionality coefficient that only depends on the applied potential V and the geometry of the channel. The gradient of the field intensity is therefore linear and reads $\nabla |E(x, V)|^2 = 2\alpha(V)^2 x$. Furthermore, the coefficient $\alpha(V)$ is also shown by the numerical simulation (note S1) to be linear with respect to the applied voltage V in the dipole limit (33). The linearity relationship reads $\alpha(V) = \beta V$, where $\beta = 1062.3 \times 10^9 \text{ m}^{-2}$ is a topography-dependent coefficient. This geometric coefficient quantifies the contribution of the step design to the shaping of the harmonic

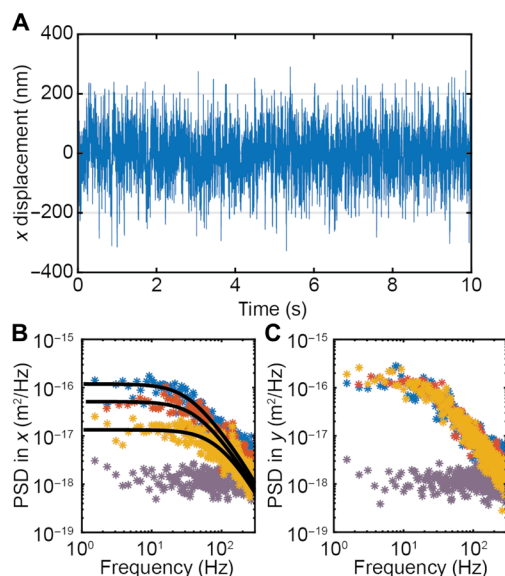


Fig. 3. Study of the motion dynamics of a confined particle. (A) Position evolution of the center of mass of the PS bead shown in Fig. 2, in the axial direction of the channel, for an electrode potential of 1.4 V. The DEP force limits the motion of the bead in-between the two valves. The time-trace exhibits the typical dynamics of a confined Brownian particle. The power spectral density (PSD) is shown in (B) and (C) for axial displacements, along the x axis and transverse displacements, along the y axis of the channel, respectively. PSDs are shown for potentials 1.4 (blue), 1.8 (red), and 2.2 V (yellow) and correspond to experiments shown in Fig. 2. The spectral noise floor (gray) is determined by analyzing the apparent displacements of an immobile PS bead on the glass ceiling over the confinement volume (electrodes off). PSDs are acquired at 1000 Hz and averaged eight times to improve readability. As shown in (B), the x dynamics follow a Lorentzian shape (fit in black lines). The roll-off frequency f_T and therefore the confinement stiffness increases with the applied voltage ($f_T = 33$ Hz for 1.4 V, $f_T = 43$ Hz for 1.8 V, and $f_T = 80$ Hz for 2.2 V). As shown in (C), the y dynamics is invariant to the external potential.

trapping potential. On the basis of the above, Eq. 1 can be written $F_{\text{DEP}}(x) = -\kappa(V)x$, where the voltage-dependent trap stiffness is

$$\kappa(V) = -4\pi\epsilon_m r^3 \text{Re}[\text{CM}]\beta^2 V^2 \quad (4)$$

Spectral analysis of the confined motion

The measured time evolution of the motion of a confined particle along x in its confinement space is presented on Fig. 3A. Imaging of the known distance between electrodes of the nanochannel calibrates the video tracking, and therefore, all extracted positions express themselves directly in meters. The graph depicts the successive positions of a confined 100-nm PS bead over 10 s with motional noise distributed around a constant mean value, typical for Brownian motion under the influence of a linear restoring force. To properly characterize the dynamics, the self-similar nature of the Brownian motion is exploited by examining its autocorrelation. This correlation is readily obtained from the power spectral density (PSD), which is the modulus of the displacement frequency of the particle squared. In the case of the Langevin equation (Eq. 3), the PSD is a Lorentzian (see note S3) function and reads (34)

$$P_{xx}(f) = \frac{D}{2\pi^2(f_T^2 + f^2)} \quad (5)$$

where $D = \frac{k_B T}{\gamma}$ is the diffusion coefficient with k_B denoting the Boltzmann constant, and $f_T = \frac{\kappa(V)}{2\pi\gamma}$ is the roll-off value of the motion frequency f . The PSD is parameterized only by the confined diffusion coefficient D and the roll-off frequency f_T , determined by fitting the experimental data based on the above expression. This enables the determination of the drag coefficient γ and the trap stiffness $\kappa(V)$ resulting from the DEP force, quantifying the strength of the confinement. A maximum likelihood estimation of $P_{xx}(f)$ is performed on the experimental spectral density to obtain D and f_T (35). The fitted PSD is corrected for low-pass filtering effects from the detection instrumentation and distortions from aliasing, which are negligible in our case (36).

Spectral densities for the x motion are presented in Fig. 3B for a set of amplitudes V ($V = 1.4$ V, $V = 1.8$ V, and $V = 2.2$ V) and nicely follow the Lorentzian shape of Eq. 5, as shown by the fitting curves (black lines). This agreement also confirms the absence of possible external contributions or an anomalous diffusion of the particle, such as chiral optical forces (37, 38) or chiral collisions with walls (39, 40), for the x motion along the channel (note S3). The position noise detection limit, shown in gray, is two orders of magnitude lower than the displacement signal at low frequencies. The resulting position resolution extracted from the noise measurement is below 10 nm. Roll-off frequencies f_T are around tens of hertz and increase with the electric field amplitude. Our setup, recording the motion at 1000 Hz, is well capable of measuring the two characteristic regimes of the PSD. At low frequencies ($f^2 \ll f_T^2$), a frequency-independent plateau is observed with value $\frac{D}{2\pi^2 f_T^2}$ that characterizes the confined motion of the nanoparticle. Steady state throughout the acquisition is verified from the displacements of the nano-objects at low frequencies strictly following the expected plateau value. In the high-frequency region ($f^2 \gg f_T^2$), the confinement is not effective anymore, and free diffusion occurs. The spectral density becomes $\frac{D}{2\pi^2 f^2}$ and follows an f^{-2} decrease proportional to the diffusion coefficient. It is worth noting that the PSD for the y motion perpendicular to the channel, shown in Fig. 3C, displays no dependency on the electrokinetic forces and imposed voltages in its spectral signatures, as expected given the absence of imposed electric field in this direction. The quality of the low-frequency plateau in the PSD determines the smallest particle that is measurable with respect to its properties, as done here. This value is determined by the polarizability of the particle, which decreases with size, the visibility given by the fluorescence signal, and the needed overall mechanical stability of the experiment, which is about 1 s for our system. Viruses were the smallest nanoparticles that we measured and characterized in this work.

Measurement of the particle hydrodynamic radius

The knowledge of the diffusion coefficient D makes the direct determination of the drag coefficient γ in the confinement region possible, as mentioned earlier. The drag force has a strong dependence on the viscosity of the fluid. In our experiments, the viscosity does not change with the ionic strength. However, because of the tight nanochannel dimensions, the particle motion reaches the close vicinity of the walls. Specifically, the particle is enclosed inside the four channel walls, which have an impact on the fluid flow generated by the moving particle and therefore affect the associated drag force. The measured drag coefficient γ is related to the Stokes drag coefficient

for freely diffusing particles in water γ_S to be able to obtain the particle hydrodynamic radius, as mentioned earlier (41–43). The introduced scaling factor Φ is parameterized by the yet unknown hydrodynamic radius r of the particle. While corrections to the drag are readily available in the absence of external forces for a particle of a known radius at a fixed position with respect to an interface (44, 45), the particle in our case moves and explores most of the confinement volume during measurements. The measured drag coefficient γ represents the averaged mobility of the particle in the channel direction x . The transverse motion in the y and z directions explores the local energy landscape (46), which accounts for the walls of the nanochannel and the corresponding electrostatic (47) and electrokinetic (18, 48) interactions with the particle. Electrokinetic forces not only confine the particle in x but also influence the particle vertical position in the z direction. The vertical density probability of positions in z contributes to the drag coefficient γ in x . However, the sensitivity of the dielectrophoretic contribution in estimating the position in the vertical z direction is dominated by the volume of the sphere ($\propto r^3$). In this direction, the interaction between the field and the particle through the conductivity is taken to be fixed with $\text{Re}[\text{CM}] = -0.25$ at 10 MHz. Using the particle probability density of positions, the hydrodynamic radius r and the scaling coefficient Φ are obtained after solving the equation $r = \Phi(r, V)\gamma/(\delta\pi\eta)$ numerically for an experimentally applied voltage V and a measured γ (note S2) (44).

The knowledge of the drag coefficient γ and the roll-off frequency f_T , extracted from the PSD, yields the trap stiffness $\kappa(V) = 2\pi\gamma f_T$. Time

traces are systematically acquired for a large number of confined PS beads with varying applied voltages V , from which the trap stiffness κ and the hydrodynamic radius r are both determined and presented on Fig. 4 (A and B, respectively). The dielectrophoretic force effecting the confinement is tuned by adjusting the potential amplitude V , as seen in Fig. 3B, resulting in varying roll-off frequencies f_T and therefore a varying trap stiffness $\kappa(V)$. A systematic study of this variation is reported in Fig. 4A and shows the evolution of the trap stiffness for PS beads (in blue) with the applied voltage V in the range from 1.3 to 2.2 V by steps of 0.1 V. For example, the trap stiffness κ for 100-nm PS beads under an applied potential of 2 V is $\kappa = 0.85$ pN/ μm . Our trap stiffnesses are comparable to those obtained using plasmonic tweezers (49, 50), but they are lower than reported values for electrostatic trapping of metallic spheres of similar sizes for very low ionic strengths ($<10^{-1}$ mM) (17, 51).

Measured hydrodynamic radii (Fig. 4B, blue points) average to $r = 51.3 \pm 12.4$ nm between 1.3 and 2 V, which is in good agreement with the manufacturer's values ($r = 50 \pm 3.15$ nm) and our own verification measurements (scanning electron microscopy images, where $r = 50.9 \pm 4.3$ nm; note S4). All error bars represent the experimental uncertainties at a 95% confidence interval (2 SDs) for a collection of particles measured at a given voltage V .

Measurement of the particle conductivity

The force $F_{\text{DEP}}(x, V)$ exerted on the particle depends on the position x of the particle and the applied electric voltage V . As mentioned earlier, with the help of numerical simulations (note S1), the nanovalve

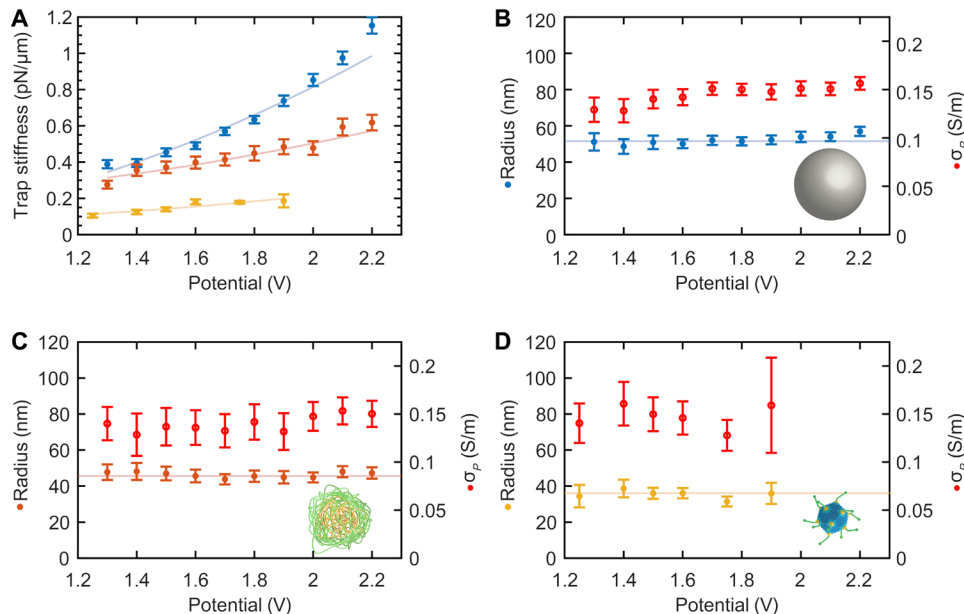


Fig. 4. Confinement stiffness, hydrodynamic radius, and conductivity. (A) The trap stiffness $\kappa(V)$ along the channel x axis of the measured 50-nm-radius PS beads (blue points), CPNs (orange points), and adenoviruses (yellow points) is shown as a function of the DEP voltage V . The stiffness increase is quadratic with the applied electric potential (fitted, solid lines). Confinement strength can be as large as 0.85 pN/ μm for 100-nm-sized dielectric PS beads. In this case, the corresponding roll-off frequency is $f_T = 67.5$ Hz. (B to D) Hydrodynamic radius and surface conductivity σ_p for PS beads, CPNs, and adenoviruses, respectively, confined and measured by the DEP trap at different DEP strengths. The hydrodynamic radius is independent of the applied potential and averages (solid lines) to be $r = 51.3 \pm 12.4$ nm, $r = 45 \pm 11.7$ nm, and $r = 36.1 \pm 7.1$ nm for PS beads, CPNs, and adenoviruses, respectively. The associated surface conductivities σ_p (red points) show little dependence on the applied potential. The conductivity values are $\sigma_p = 0.15 \pm 0.04$ S/m, $\sigma_p = 0.14 \pm 0.06$ S/m, and $\sigma_p = 0.15 \pm 0.04$ S/m for PS beads, CPNs, and adenoviruses, respectively. All error bars represent the experimental uncertainties at a 95% confidence interval (2 SDs) for a collection of particles at a given voltage V . Typically, the number of points N at $V = 1.6$ V is $N = 79$, $N = 40$, and $N = 13$ for PS beads, CPNs, and adenoviruses, respectively.

topography is designed such that the dielectrophoretic force in the confinement region is linear in the x direction, and the trap stiffness is proportional to the square of the applied potential V (Eq. 4). For PS beads, this is confirmed in Fig. 4A, where the trap stiffness exhibits a quadratic behavior (best fit in blue line) with respect to V . Data points at 1.3 V and above 2 V depart slightly from this trend. Low voltages allow the beads to explore a wider confinement space, sometimes partially escaping and then returning to the center of the confinement region. On the contrary, beads trapped at high voltages are so tightly confined that their PSD motion approaches the detection limit noise, in particular at high frequencies. As the background noise contributes to the overall signal amplitude, estimation of dynamical parameters becomes biased. This is clearly apparent in Fig. 3B for $V = 2.2$ V, where the roll-off frequency is $f_r = 80$ Hz. At this frequency, the background noise contributes already one-tenth of the PSD, rendering a proper estimation in the high-frequency region difficult. Therefore, experiments at low and high V define the limits of validity for our approach, i.e., the bounds of the region where the dielectrophoretic force is linear and significantly over the motion noise, allowing a reliable determination of the nano-objects properties.

With a chosen applied electric potential V and an already determined hydrodynamic radius r , the measured trap stiffness $\kappa(V)$ (Eq. 4) only depends on the real part of the CM factor, $\text{Re}[CM]$, which can thus be determined. This also yields the particle conductivity $\sigma_p = \frac{\sigma_m(2\text{Re}[CM]+1)}{1-\text{Re}[CM]}$ from Eq. 1, with the ionic strength of the solution set at a medium conductivity of $\sigma_m = 0.24$ S/m. The high ionic strength of the medium is associated with a thin double layer that allows the determination of the conductivity with the previous expression, for a range of frequencies before the transition region and above very low frequencies where ionic flows will play a role (see note S1, fig. S4). Measurement of the trap stiffness provides a direct estimation of the polarizability of the particle. If extraction of particle properties is desired out of experiments performed with very low electric field frequencies and in fluids of lower ionic concentrations, then additional electro-osmotic contributions to the polarizability must be considered (31, 32). The conductivity of the 100-nm PS beads (in $0.1 \times$ PBS) is shown in Fig. 4B (red points) for different voltages. It is, as expected, found to be voltage independent and has a mean value $\sigma_p = 0.15 \pm 0.04$ S/m. Radius and conductivity measurements are constant with varying the potential amplitude V . This is expected from Eq. 4 where the radius r and conductivity σ_p contributions to the force are multiplicative factors without V dependency. Constancy of r and σ_p with respect to V also confirms the harmonic nature of the confining potential and the validity of the underlying assumptions in obtaining Eq. 4 (notes S1 and S2).

Studying known property PS nanospheres shows that a careful analysis of the confined particle motion dynamics results in the determination of a host of important particle properties. Next, we venture into unknown property nano-objects, relevant to biological applications, namely, CPNs and adenoviruses, and target the determination of the same properties.

Characterization of CPNs and adenoviruses

CPNs are a family of macromolecules with large delocalized π -conjugated backbones. Compared to quantum dots, they show lower cytotoxicity, high photostability, high fluorescence, and no blinking (52–55), making them favorable for a variety of biological applications.

Their strong optoelectronic performances (54, 56) and fluorescence allow their use for combined diagnostics and treatment, in therapeutics applications (56, 57). Manipulation and characterization of CPNs at the single-entity level has not been yet reported, to the best of our knowledge. Furthermore, we study adenoviruses. They are common pathogens in humans and animals. The ability to control and study them individually can help in the challenging determination of their infection pathway (58–60).

The CPNs are found to be well confined by the electrokinetic forces, similar to PS beads, even though their fluorescence is weaker. The roll-off frequencies and diffusion coefficients are measured from PSDs (note S5) to determine the CPNs' hydrodynamic radius and electrical conductivity, which are presented in Fig. 4C for varying electric voltages. The measurements are voltage invariant, and the mean values are estimated from all measurements between 1.3 and 2.0 V. The confinement of CPNs has a typical trap stiffnesses of $\kappa = 0.48$ pN/ μm at 2 V. The CPN hydrodynamic radius averages to $r = 45 \pm 11.7$ nm, while their electrical conductivity has a value of $\sigma_p = 0.14 \pm 0.06$ S/m. The CPN suspension is relatively homogeneous with respect to particle size, and the dispersion around the mean is small. This makes these particles practically suited for controlled applications in biological environments such as drug delivery in small capillaries and light activated local heating.

The adenoviruses (AdV-TS1) are grown in vitro and are doped with fluorescent dyes (Alexa Fluor 488 5-TFP amine reactive dye). The viruses are trapped and investigated for voltage amplitudes between 1.25 and 1.9 V. The confinement of the viruses is found to be stable (note S5), with a typical trap stiffness of $\kappa = 0.2$ pN/ μm at 1.9 V. One measurement (for each electrical potential) could be performed per virus, before the fluorescence signal decreases because of particle bleaching, which hinders further detection. Spectral densities were computed from time traces recorded at 500 Hz, resulting in a measured mean hydrodynamic radius of $r = 36.1 \pm 7.1$ nm and a mean electrical conductivity of $\sigma_p = 0.15 \pm 0.04$ S/m. While the determined measurement values and error bars for viruses are reasonable throughout our experiments, the statistics of these particular experiments is somewhat limited compared to PS beads and CPNs, averaging to 10 data points per voltage.

The measured in situ hydrodynamic radius is in good agreement with size measurements of similar adenoviruses but in a different environment, using electron microscopy (61, 62). Conductivity measurements of the individual viruses are also comparable to average values obtained for other viruses with ensemble measurements. Values for the conductivity of larger (200 nm) herpes simplex viruses, at lower ionic concentrations, are reported to be 0.1 S/m (63). The tobacco mosaic virus has a rod shape (length of 280 nm for a width of only 18 nm) and a reported larger conductivity of 0.4 S/m (64). The adenoviruses and previously uncharacterized synthetic CPNs of the present work are found to have limited size disparity. Our experimental approach can be very useful in determining size and related property disparity with single-entity resolution, not amenable to ensemble methods but important to biological bio-objects, in our quest to understand mechanisms of processes such as infectivity (65).

DISCUSSION

We have shown that the on-chip, rational design of an electrokinetic nanovalve system with a linearly restoring trapping mechanism,

combined with the analysis of the resulting, judiciously restricted, particle motion dynamics, enables the determination, within seconds, of a host of important properties of dielectric and biological nano-objects smaller than a hundred nanometers, at biological level ionic concentrations. PS beads and unknown property biological nanoparticles (CPNs and adenoviruses) are controlled and characterized at the individual particle level. The present platform is a substantial advancement supplementing existing approaches, such as optical spectroscopy (66), aiming at advancing fundamental knowledge and applications involving a broad range of nanoscale matter operating in liquids.

METHODS

Preparation of biological and synthetic particles

Carboxylated PS beads of mean diameter of 100 ± 6.3 nm from Thermo Fisher Scientific (FluoSpheres, F8803) are used for the experiments. The beads are loaded with a proprietary dye, a fluorescent molecule with an absorption peak at 505 nm and an emission peak at 515 nm. The initial concentration of 2% solids was diluted 1:200 to obtain a $0.1 \times$ PBS concentration (Gibco).

CPNs (CPN 510, Stream Bio) with an advertised hydrodynamic radius of 80 nm are also used. The particles exhibit an emission peak at 510 nm with an absorption peak at 450 nm. The initial concentration of 0.1 mg/ml was diluted 1:100 with buffered saline (PBS, Gibco) and deionized water to achieve a $0.1 \times$ buffer concentration.

Solution of adenoviruses, HAdV-C2_T51, was prepared the same way as previously reported (18). The particles exhibit an emission peak at 525 nm with an absorption peak at 488 nm. The solution was diluted with PBS (Gibco), bovine serum albumin (BSA; Sigma-Aldrich), and deionized water to achieve a solution with $0.1 \times$ PBS and 5 weight % BSA concentration.

SUPPLEMENTARY MATERIALS

Supplementary material for this article is available at <http://advances.sciencemag.org/cgi/content/full/7/27/eabd8758/DC1>

[View/request a protocol for this paper from Bio-protocol.](#)

REFERENCES AND NOTES

1. Y. Pang, H. Song, J. H. Kim, X. Hou, W. Cheng, Optical trapping of individual human immunodeficiency viruses in culture fluid reveals heterogeneity with single-molecule resolution. *Nat. Nanotechnol.* **9**, 624–630 (2014).
2. U. F. Greber, M. Way, A superhighway to virus infection. *Cell* **124**, 741–754 (2006).
3. K. Cho, X. Wang, S. Nie, Z. Chen, D. M. Shin, Therapeutic nanoparticles for drug delivery in cancer. *Clin. Cancer Res.* **14**, 1310–1316 (2008).
4. E. Amstad, E. Reimhult, Nanoparticle actuated hollow drug delivery vehicles. *Nanomedicine* **7**, 145–164 (2012).
5. C. A. Aguilar, H. G. Craighead, Micro- and nanoscale devices for the investigation of epigenetics and chromatin dynamics. *Nat. Nanotechnol.* **8**, 709–718 (2013).
6. C. S. S. R. Kumar, *Nanotechnology Characterization Tools for Biosensing and Medical Diagnosis* (Springer-Verlag Berlin Heidelberg, 2018).
7. J. Li, B. E.-F. de Ávila, W. Gao, L. Zhang, J. Wang, Micro/nanorobots for Biomedicine: Delivery, surgery, sensing, and detoxification. *Sci. Robot.* **2**, eaam6431 (2017).
8. A. Ghosh, P. Fischer, Controlled propulsion of artificial magnetic nanostructured propellers. *Nano Lett.* **9**, 2243–2245 (2009).
9. M.-C. Daniel, D. Astruc, Gold nanoparticles: Assembly, supramolecular chemistry, quantum-size-related properties, and applications toward biology, catalysis, and nanotechnology. *Chem. Rev.* **104**, 293–346 (2004).
10. B. H. Wunsch, J. T. Smith, S. M. Gifford, C. Wang, M. Brink, R. L. Bruce, R. H. Austin, G. Stolovitzky, Y. Astier, Nanoscale lateral displacement arrays for the separation of exosomes and colloids down to 20nm. *Nat. Nanotechnol.* **11**, 936–940 (2016).
11. W. Wu, X. Zhu, Y. Zuo, L. Liang, S. Zhang, X. Zhang, Y. Yang, Precise sorting of gold nanoparticles in a flowing system. *ACS Photonics*. **3**, 2497–2504 (2016).
12. G. Tkachenko, E. Brasselet, Optofluidic sorting of material chirality by chiral light. *Nat. Commun.* **5**, 3577 (2014).
13. A. Cuche, A. Canaguier-Durand, E. Devaux, J. A. Hutchison, C. Genet, T. W. Ebbesen, Sorting nanoparticles with intertwined plasmonic and thermo-hydrodynamical forces. *Nano Lett.* **13**, 4230–4235 (2013).
14. H. Morgan, N. G. Green, *AC Electrokinetics: Colloids and Nanoparticles* (Research Studies Press, 2003).
15. Y. Pang, R. Gordon, Optical trapping of 12 nm dielectric spheres using double-nanoholes in a gold film. *Nano Lett.* **11**, 3763–3767 (2011).
16. C. Hong, S. Yang, J. C. Ndukaife, Stand-off trapping and manipulation of sub-10 nm objects and biomolecules using opto-thermo-electrohydrodynamic tweezers. *Nat. Nanotechnol.* **15**, 908–913 (2020).
17. M. Krishnan, N. Mojarad, P. Kukura, V. Sandoghdar, Geometry-induced electrostatic trapping of nanometric objects in a fluid. *Nature* **467**, 692–695 (2010).
18. P. Eberle, C. Höller, P. Müller, M. Suomalainen, U. F. Greber, H. Eghlidi, D. Poulikakos, Single entity resolution valving of nanoscopic species in liquids. *Nat. Nanotechnol.* **13**, 578–582 (2018).
19. M. J. Skaug, C. Schwemmer, S. Fringes, C. D. Rawlings, A. W. Knoll, Nanofluidic rocking Brownian motors. *Science* **359**, 1505–1508 (2018).
20. N. Mojarad, V. Sandoghdar, M. Krishnan, Measuring three-dimensional interaction potentials using optical interference. *Opt. Express* **21**, 9377–9389 (2013).
21. F. Ruggeri, F. Zosel, N. Mutter, M. Rozycka, M. Wojtas, A. Ozyhar, B. Schuler, M. Krishnan, Single-molecule electrometry. *Nat. Nanotechnol.* **12**, 488–495 (2017).
22. R. J. P. Williams, *The Natural Selection of the Chemical Elements* (Clarendon Press, 1997), vol. 53.
23. R. R. Henriquez, T. Ito, L. Sun, R. M. Crooks, The resurgence of coulter counting for analyzing nanoscale objects. *Analyst* **129**, 478–482 (2004).
24. Y. Song, J. Zhang, D. Li, Microfluidic and nanofluidic resistive pulse sensing: A review. *Micromachines* **8**, 204 (2017).
25. H. Morgan, M. P. Hughes, N. G. Green, Separation of submicron bioparticles by dielectrophoresis. *Biophys. J.* **77**, 516–525 (1999).
26. A. Bariq, Y. Zhang, R. Grassi, B. P. Nadappuram, J. B. Edel, T. Low, S. J. Koester, S.-H. Oh, Graphene-edge dielectrophoretic tweezers for trapping of biomolecules. *Nat. Commun.* **8**, 1867 (2017).
27. A. E. Cohen, W. E. Moerner, Suppressing Brownian motion of individual biomolecules in solution. *Proc. Natl. Acad. Sci. U.S.A.* **103**, 4362–4365 (2006).
28. G. Baffou, R. Quidant, Thermo-plasmonics: Using metallic nanostructures as nano-sources of heat. *Laser Photonics Rev.* **7**, 171–187 (2013).
29. L. Wang, A. K. Gaigalas, V. Reipa, Optical properties of Alexa™ 488 and Cy™5 immobilized on a glass surface. *Biotechniques* **38**, 127–132 (2005).
30. F. Aguet, C. N. Antonescu, M. Mettlen, S. L. Schmid, G. Danuser, Advances in analysis of low signal-to-noise images link dynamin and AP2 to the functions of an endocytic checkpoint. *Dev. Cell* **26**, 279–291 (2013).
31. H. Zhou, M. A. Preston, R. D. Tilton, L. R. White, Calculation of the electric polarizability of a charged spherical dielectric particle by the theory of colloidal electrokinetics. *J. Colloid Interface Sci.* **285**, 845–856 (2005).
32. H. Zhao, On the effect of hydrodynamic slip on the polarization of a nonconducting spherical particle in an alternating electric field. *Phys. Fluids* **22**, 072004 (2010).
33. M. Washizu, T. B. Jones, Generalized multipolar dielectrophoretic force and electrorotational torque calculation. *J. Electrostat.* **38**, 199–211 (1996).
34. K. Berg-Sørensen, H. Flyvbjerg, Power spectrum analysis for optical tweezers. *Rev. Sci. Instrum.* **75**, 594–612 (2004).
35. S. F. Nørrelykke, H. Flyvbjerg, Power spectrum analysis with least-squares fitting: Amplitude bias and its elimination, with application to optical tweezers and atomic force microscope cantilevers. *Rev. Sci. Instrum.* **81**, 075103 (2010).
36. B. M. Lansdorp, O. A. Saleh, Power spectrum and Allan variance methods for calibrating single-molecule video-tracking instruments. *Rev. Sci. Instrum.* **83**, 025115 (2012).
37. A. Canaguier-Durand, J. A. Hutchison, C. Genet, T. W. Ebbesen, Mechanical separation of chiral dipoles by chiral light. *New J. Phys.* **15**, 123037 (2013).
38. R. P. Cameron, S. M. Barnett, A. M. Yao, Discriminatory optical force for chiral molecules. *New J. Phys.* **16**, 013020 (2014).
39. L. Caprini, U. M. B. Marconi, Active chiral particles under confinement: Surface currents and bulk accumulation phenomena. *Soft Matter* **15**, 2627–2637 (2019).
40. T. Barois, J.-F. Boudet, J. S. Lintuvuori, H. Kellay, Sorting and extraction of self-propelled chiral particles by polarized wall currents. *Phys. Rev. Lett.* **125**, 238003 (2020).
41. J. Leach, H. Mushfique, S. Keen, R. Di Leonardo, G. Ruocco, J. M. Cooper, M. J. Padgett, Comparison of Faxén's correction for a microsphere translating or rotating near a surface. *Phys. Rev. E* **79**, 026301 (2009).

42. A. J. Goldman, R. G. Cox, H. Brenner, Slow viscous motion of a sphere parallel to a plane wall—II Couette flow. *Chem. Eng. Sci.* **22**, 653–660 (1967).
43. H. Faxén, Die Bewegung einer starren Kugel langs der Achse eines mit zäher Flüssigkeit gefüllten Rohres. *Ark. Matematik Astron. och Fys.* **17**, 1–28 (1923).
44. M. I. M. Feitosa, O. N. Mesquita, Wall-drag effect on diffusion of colloidal particles near surfaces: A photon correlation study. *Phys. Rev. A* **44**, 6677–6685 (1991).
45. S. Fringes, F. Holzner, A. W. Knoll, The nanofluidic confinement apparatus: Studying confinement-dependent nanoparticle behavior and diffusion. *Beilstein J. Nanotechnol.* **9**, 301–310 (2018).
46. Y. Pawar, J. L. Anderson, Hindered diffusion in slit pores: An analytical result. *Ind. Eng. Chem. Res.* **32**, 743–746 (1993).
47. P. K. Das, S. Bhattacharjee, Electrostatic double layer force between a sphere and a planar substrate in the presence of previously deposited spherical particles. *Langmuir* **21**, 4755–4764 (2005).
48. R. Pethig, in *Dielectrophoresis* (John Wiley & Sons Ltd, 2017).
49. G. Volpe, R. Quidant, G. Badenes, D. Petrov, Surface plasmon radiation forces. *Phys. Rev. Lett.* **96**, 238101 (2006).
50. A. N. Grigorenko, N. W. Roberts, M. R. Dickinson, Y. Zhang, Nanometric optical tweezers based on nanostructured substrates. *Nat. Photonics.* **2**, 365–370 (2008).
51. M. Celebrano, C. Rosman, C. Sönnichsen, M. Krishnan, Angular trapping of anisometric nano-objects in a fluid. *Nano Lett.* **12**, 5791–5796 (2012).
52. A. L. Efros, D. J. Nesbitt, Origin and control of blinking in quantum dots. *Nat. Nanotechnol.* **11**, 661–671 (2016).
53. Y. Braeken, S. Cheruku, A. Ethirajan, W. Maes, Conjugated polymer nanoparticles for bioimaging. *Materials* **10**, 1420 (2017).
54. T. F. Abelha, T. W. Phillips, J. H. Bannock, A. M. Nightingale, C. A. Dreiss, E. Kemal, L. Urbano, J. C. Demello, M. Green, L. A. Dailey, Bright conjugated polymer nanoparticles containing a biodegradable shell produced at high yields and with tuneable optical properties by a scalable microfluidic device. *Nanoscale* **9**, 2009–2019 (2017).
55. L. Feng, C. Zhu, H. Yuan, L. Liu, F. Lv, S. Wang, Conjugated polymer nanoparticles: Preparation, properties, functionalization and biological applications. *Chem. Soc. Rev.* **42**, 6620–6633 (2013).
56. C.-g. Qian, Y.-l. Chen, P.-j. Feng, X.-z. Xiao, M. Dong, J.-c. Yu, Q.-y. Hu, Q.-d. Shen, Z. Gu, Conjugated polymer nanomaterials for theranostics. *Acta Pharmacol. Sin.* **38**, 764–781 (2017).
57. Y. Wang, L. Feng, S. Wang, Conjugated polymer nanoparticles for imaging, cell activity regulation, and therapy. *Adv. Funct. Mater.* **29**, 1806818 (2019).
58. M. Lakadamyali, M. J. Rust, H. P. Babcock, X. Zhuang, Visualizing infection of individual influenza viruses. *Proc. Natl. Acad. Sci. U.S.A.* **100**, 9280–9285 (2003).
59. U. F. Greber, J. W. Flatt, Adenovirus entry: From infection to immunity. *Annu. Rev. Virol.* **6**, 177–197 (2019).
60. U. F. Greber, Adenoviruses – Infection, pathogenesis and therapy. *FEBS Lett.* **594**, 1818–1827 (2020).
61. V. S. Reddy, S. K. Natchiar, P. L. Stewart, G. R. Nemerow, Crystal structure of human adenovirus at 3.5 Å resolution. *Science* **329**, 1071–1075 (2010).
62. H. Liu, L. Jin, S. B. S. Koh, I. Atanasov, S. Schein, L. Wu, Z. H. Zhou, Atomic structure of human adenovirus by cryo-EM reveals interactions among protein networks. *Science* **329**, 1038–1043 (2010).
63. M. P. Hughes, H. Morgan, F. J. Rixon, Measuring the dielectric properties of herpes simplex virus type 1 virions with dielectrophoresis. *Biochim. Biophys. Acta Gen. Subj.* **1571**, 1–8 (2002).
64. I. Ermolina, H. Morgan, N. G. Green, J. J. Milner, Y. Feldman, Dielectric spectroscopy of Tobacco Mosaic Virus. *Biochim. Biophys. Acta Gen. Subj.* **1622**, 57–63 (2003).
65. G. Seisenberger, M. U. Ried, T. Endress, H. Büning, M. Hallek, C. Bräuchle, Real-time single-molecule imaging of the infection pathway of an adeno-associated virus. *Science* **294**, 1929–1932 (2001).
66. A. H. Squires, P. D. Dahlberg, H. Liu, N. C. M. Magdaong, R. E. Blankenship, W. E. Moerner, Single-molecule trapping and spectroscopy reveals photophysical heterogeneity of phycobilisomes quenched by orange carotenoid protein. *Nat. Commun.* **10**, 1172 (2019).

Acknowledgments

Funding: The work was supported partially by the Swiss National Foundation under grants 200021_162855 and 31003A_179256. **Author contributions:** D.P. and H.E. had the original idea of the project. D.P., G.S., and H.E. designed research and provided scientific advice throughout the project. C.H. fabricated the devices and performed experiments. G.S. and C.H. developed the theory and experimental approach for characterization. C.H. and G.S. analyzed the data. M.S. and U.F.G. provided adenoviruses and expertise on viral particles. G.S., C.H., and D.P. wrote the paper. All authors read the paper draft and provided useful comments and revisions. **Competing interests:** The authors declare that they have no competing interests. **Data and materials availability:** All data needed to evaluate the conclusions in the paper are present in the paper and/or the Supplementary Materials. Additional data related to this paper may be requested from the authors.

Submitted 18 August 2020

Accepted 19 May 2021

Published 2 July 2021

10.1126/sciadv.abd8758

Citation: C. Höller, G. Schnoering, H. Eghlidi, M. Suomalainen, U. F. Greber, D. Poulikakos, On-chip transporting arresting and characterizing individual nano-objects in biological ionic liquids. *Sci. Adv.* **7**, eabd8758 (2021).

On-chip transporting arresting and characterizing individual nano-objects in biological ionic liquids

Christian Höller, Gabriel Schnoering, Hadi Eghlidi, Maarit Suomalainen, Urs F. Greber and Dimos Poulikakos

Sci Adv 7 (27), eabd8758.
DOI: 10.1126/sciadv.abd8758

ARTICLE TOOLS	http://advances.sciencemag.org/content/7/27/eabd8758
SUPPLEMENTARY MATERIALS	http://advances.sciencemag.org/content/suppl/2021/06/28/7.27.eabd8758.DC1
REFERENCES	This article cites 62 articles, 7 of which you can access for free http://advances.sciencemag.org/content/7/27/eabd8758#BIBL
PERMISSIONS	http://www.sciencemag.org/help/reprints-and-permissions

Use of this article is subject to the [Terms of Service](#)

Science Advances (ISSN 2375-2548) is published by the American Association for the Advancement of Science, 1200 New York Avenue NW, Washington, DC 20005. The title *Science Advances* is a registered trademark of AAAS.

Copyright © 2021 The Authors, some rights reserved; exclusive licensee American Association for the Advancement of Science. No claim to original U.S. Government Works. Distributed under a Creative Commons Attribution NonCommercial License 4.0 (CC BY-NC).